Atmospheric Research 260 (2021) 105626

Contents lists available at ScienceDirect

Atmospheric Research

journal homepage: www.elsevier.com/locate/atmosres

The global electric circuit land–ocean response to the El Niño—Southern Oscillation

Nikolay N. Slyunyaev [a,*], Nikolay V. Ilin [a], Evgeny A. Mareev [a], Colin G. Price [a,b]

[a] Institute of Applied Physics, Russian Academy of Sciences, 46 Ulyanova St., 603950 Nizhny Novgorod, Russia
[b] Department of Geophysics, Porter School of the Environment and Earth Sciences, Tel Aviv University, 20 Levanon Rd., Tel Aviv 6997801, Israel

ARTICLE INFO

Keywords:
Global electric circuit
Ionospheric potential
ENSO
Convection
Modelling
Land–ocean contrast

ABSTRACT

It is known that the global electric circuit (GEC) intensity can be characterised by a single global index, namely the ionospheric potential (IP), made up of contributions from electrified clouds all over the globe. Using the Weather Research and Forecasting model, we have reproduced the atmospheric dynamics for 2008–2018 and simulated the variation of the GEC by parameterising regional contributions to the IP in terms of convection and precipitation. Considering that the El Niño—Southern Oscillation (ENSO) can be quantitatively characterised by sea surface temperatures (SSTs) in the Niño 3.4 region, this allowed us to identify and study in detail the effect of ENSO on regional contributions to the GEC. Our simulations have shown that contributions to the GEC from the land and oceanic parts of the Earth's surface respond oppositely to the ENSO cycle. The oceanic contribution is positively correlated with the Niño 3.4 SST, largely owing to increases in convection over the Pacific Ocean. In contrast to the oceans, the land contribution shows a negative correlation with ENSO due to decreases in convection over the Maritime Continent and South America. The observed correlations are statistically significant and are clearly seen on the decadal timescale; at the same time contributions to the IP for individual years do not always clearly reflect the corresponding Niño 3.4 SST anomalies. During the two El Niños and two La Niñas that occurred between 2008 and 2018, the oceanic contribution always changed in phase with ENSO, increasing in El Niño years and decreasing in La Niña years; on the other hand, the contribution of land showed a clear variation in antiphase with ENSO only for the 2015/16 El Niño and 2010/11 La Niña, characterised by extremely large SST anomalies, with a small and indefinite effect for the two lesser events. When summing the contributions of land and ocean, two strong effects of opposite signs nearly counterbalance each other and we obtain a much less pronounced effect of ENSO on the total IP. This effect is generally positive since land and ocean provide nearly equal contributions to the GEC during Northern Hemisphere winters and, according to our analysis, the contribution of ocean is slightly more sensitive to ENSO than that of land.

1. Introduction

The El Niño—Southern Oscillation (ENSO) is the largest cause of climate variations on Earth after the seasonal cycle of summer and winter. The ENSO is made up of irregular cycles, each of which contains a warm phase (El Niño) and a cold phase (La Niña), driven by changes in sea surface temperatures (SSTs) in the central and eastern equatorial Pacific Ocean (see, e.g., McPhaden et al., 2020). During ENSO events the SSTs in the eastern Pacific increase (in the case of El Niños) or decrease (in the case of La Niñas) by a few degrees for extended periods of 12–18 months. These SST changes occur over very large areas for extended periods of time and hence have a direct influence on the global climate system with major impacts on global temperature patterns (Tsonis et al., 2005) and global rainfall patterns (Villafuerte II and Matsumoto, 2015).

It is thought that most of these changes are related to shifts in the atmospheric convection patterns. Both the north—south Hadley circulation and the east—west Walker circulation shift during ENSO events, with implications on the hydrological cycle around the globe. These circulation patterns are related to tropical deep convection, which is often associated with thunderstorms and lightning activity. Therefore it is clear that the ENSO cycle has a substantial influence on the Earth's electrical environment; this influence has been discussed in a number of studies, whose review can be found in Williams and Mareev (2014, section 9). Nearly all of these studies investigated the impact of ENSO on

* Corresponding author.
E-mail address: slyunyaev.n@ipfran.ru (N.N. Slyunyaev).

https://doi.org/10.1016/j.atmosres.2021.105626
Received 22 December 2020; Received in revised form 10 March 2021; Accepted 8 April 2021
Available online 20 April 2021
0169-8095/© 2021 Elsevier B.V. All rights reserved.

lightning activity (e.g., Sátori and Zieger, 1999; Goodman et al., 2000; Hamid et al., 2001; Price and Federmesser, 2006; Sátori et al., 2009; Price, 2009). However, such investigations were generally focused on specific regions and no global analysis has been performed; this is due to the lack of global data related to thunderstorms and electrified clouds on long timescales needed to study ENSO variability.

Despite a considerable amount of research devoted to investigating the effect of ENSO on lightning, little attention has been given to its impact on quasi-stationary fields and currents in the atmosphere. At the same time it is known that such fields and currents are part of the so-called global electric circuit (GEC; see, e.g., Rycroft et al., 2000; Tinsley, 2008), which is a natural concept to consider when analysing global effects of climate variations on atmospheric electricity. The idea of the GEC is based on the hypothesis proposed by Wilson (1921, 1924) according to which the charging of thunderstorms and electrified shower clouds (ESCs) maintains the distribution of quasi-stationary fields and currents in the entire atmosphere. More precisely, it is thought that charge separation inside electrified clouds (both thunderstorms and ESCs) drives the electric current upwards to the ionosphere (Mach et al., 2010, 2011), and this current eventually returns to the Earth's surface in fair-weather regions (e.g., deserts). The highly conducting (hence nearly equipotential) Earth and ionosphere complete the electrical network; the potential difference between them is called the ionospheric potential (IP; Markson, 1986, 2007).

Thus the GEC links together thundestorm regions and fair-weather regions. Experimental evidence supporting this concept includes the well-known observation that the diurnal variation of the fair-weather electric field at the Earth's surface in universal time (UTC) looks nearly the same at different locations around the globe (this dependence is called the Carnegie curve; see Harrison, 2013) and is tightly correlated with the diurnal cycle of global thunderstorm activity (Whipple and Scrase, 1936). Another observation corroborating the concept of the GEC is the fact that simultaneous measurements of the IP (i.e. of the potential of the lower ionosphere relative to the Earth's surface) performed at remote locations yield similar results (Markson et al., 1999), which suggests that the lower ionosphere indeed has the same potential all over the globe, maintained by global thunderstorms and ESCs.

Until recently, the only known study aimed at investigating the effect of ENSO on the GEC was the one by Harrison et al. (2011), who analysed the results of atmospheric electricity measurements at the Shetland Islands during 1968–1984. They found a positive correlation between the mean fair-weather potential gradient in December and the ENSO cycle and identified the hours when the potential gradient is most sensitive to ENSO variability. However, atmospheric electricity measurements are not able to reveal the mechanisms behind the observed links between ENSO and the GEC, as the measured potential gradient values are determined by the sum of contributions to the GEC from electrified clouds all over the globe and it is impossible to determine which regions contributed the most to this value.

In this regard, it is particularly helpful to employ theoretical modelling. Global models of atmospheric dynamics can both provide ENSO indices of SST and surface pressure anomalies (e.g., Southern Oscillation Index) and simulate the convection in response to changes in these SSTs. In addition, recent studies (Slyunyaev et al., 2019; Ilin et al., 2020) have developed a methodology of estimating the spatial and temporal distribution of electrified clouds in these models and their contributions to the GEC. Recently Slyunyaev et al. (2021) have employed this approach to identify the influence of ENSO on the shape of the diurnal variation of the GEC; in particular, they have shown that pronounced anomalies in the relative IP around 13:00 UTC and 21:00 UTC precisely correspond to strong El Niño and La Niña events.

In this study we present another link between ENSO variability and changes in the IP (which characterises the GEC intensity). Instead of regarding the IP as a single integrated global quantity, we focus on contributions to the total IP from different regions of the globe. Using the Weather Research and Forecasting model (WRF; see Skamarock et al., 2008), we reproduce the global atmospheric dynamics on the basis of real meteorological data over a decade covering several ENSO events. Then a parameterisation of the IP allows us to investigate the impact of ENSO on regional contributions to the GEC and to reveal the cumulative effect of all such regional links, thereby elucidating the relationship between ENSO and the GEC.

2. Simulation of the GEC

To simulate the GEC, we employ a procedure similar to that described in Ilin et al. (2020) and Slyunyaev et al. (2021). Here we give only a very brief summary of the detailed description. First, we simulate atmospheric dynamics on every third day during the years 2008–2018 by means of the globally running WRF model on a $1^\circ \times 1^\circ$ latitude-longitude grid with 51 altitude levels. More precisely, we perform free runs of the WRF, initialising the model with meteorological reanalysis data based on actual observations (National Centers for Environmental Prediction, National Weather Service, NOAA and U.S. Department of Commerce, 2000). Next, on the same days for which we simulated atmospheric dynamics we calculate the IP by employing a parameterisation based on cutting off the grid columns with weak convective activity and estimating the area occupied by electrified clouds in each column from the amount of precipitation (Mareev and Volodin, 2014; Ilin et al., 2020). Finally, the diurnal variation of the GEC is obtained by averaging hourly IP values over a large number of days and 'regularising' them by adding a suitable linear function of time (while keeping the diurnal mean value the same); such a regularisation is required to compensate for systematic modelling uncertainties caused by using free runs of the WRF (Ilin et al., 2020).

Technical details of the GEC simulation procedure briefly described above can be found in Ilin et al. (2020) and Slyunyaev et al. (2021). Here we refrain from their detailed description and discussion; however, the formula used to estimate the IP in terms of atmospheric parameters is given in Appendix A. By restricting the sum in this formula to the grid columns pertaining to specific regions of the Earth's surface, we can simulate contributions to the total IP from these regions and study their variability on different time scales.

In this paper we investigate the effect of ENSO on the GEC; considering that peaks of El Niño and La Niña events usually occur around December, here we restrict our attention to the 5-month periods around Decembers. Since we have simulated the atmospheric dynamics and the GEC for 2008–2018, we consider the ten October—February periods that occured during this time span (2008/09, 2009/10, etc.). These ten periods will make it possible to look at strong El Niño events in 2009/10 and 2015/16 and strong La Niña events in 2010/11 and 2011/12; of these four events the 2015/16 El Niño was particularly intense.

The parameterisation of the IP that we use (see Eq. (A.1)) contains the factor j_0, representing the characteristic value of the charge separation current density inside thunderstorms and electrified shower clouds (which serve as GEC generators). Given that there is virtually no experimental data on charge separation currents inside electrified clouds (note that the Wilson current above a cloud may be substantially different from the charging current inside it owing to the finite resistance of the cloud), we can only choose the value of j_0 by requiring that certain global parameters have reasonable values. Here we normalise all contributions to the IP such that the mean total averaged over October—February periods of 2008/09–2017/18 is equal to 240 kV, which is a rather typical value for the IP (Markson, 2007). Note that when we look at the IP variation (i.e. compare the IP values at different moments of time), this normalisation does not influence our conclusions, but it is often more convenient to express the IP in volts rather than as a fraction of some long-term mean value.

It turns out that the approach to simulating the GEC described above allows one to reproduce the shape of the annual average Carnegie curve, but tends to underestimate its peak-to-peak amplitude (Slyunyaev et al., 2019). It should be emphasised that this is not a shortcoming of this particular parameterisation; similar underestimation of amplitude was observed in other studies aimed at predicting the diurnal variation of the GEC by parameterising contributions from electrified clouds in weather forecasting or climate models (Mareev and Volodin, 2014; Lucas et al., 2015; Kalb et al., 2016; Jánský et al., 2017). This disagreement is a result of the inability of large-scale models to thoroughly distinguish between electrified clouds (which alone serve as GEC generators) and non-electrified clouds. However, as we have already noted, here we concentrate on October—February periods, during which the impact of ENSO is most prominent; at the same time it is known that during Northern Hemisphere winters the diurnal variation of the GEC predicted by large-scale simulations is closer to the classical Carnegie curve (with a 24-h sample correlation coefficient of about 0.98), and the underestimation of the peak-to-peak amplitude is less pronounced (Ilin et al., 2020). This justifies using large-scale simulations to investigate the links between ENSO and the GEC; another argument in favour of this approach is that we are going to analyse changes in contributions to the GEC from different regions during strong El Niños and La Niñas, whereas systematic overestimation or underestimation of the contribution to the GEC from a particular region should not affect general trends observed

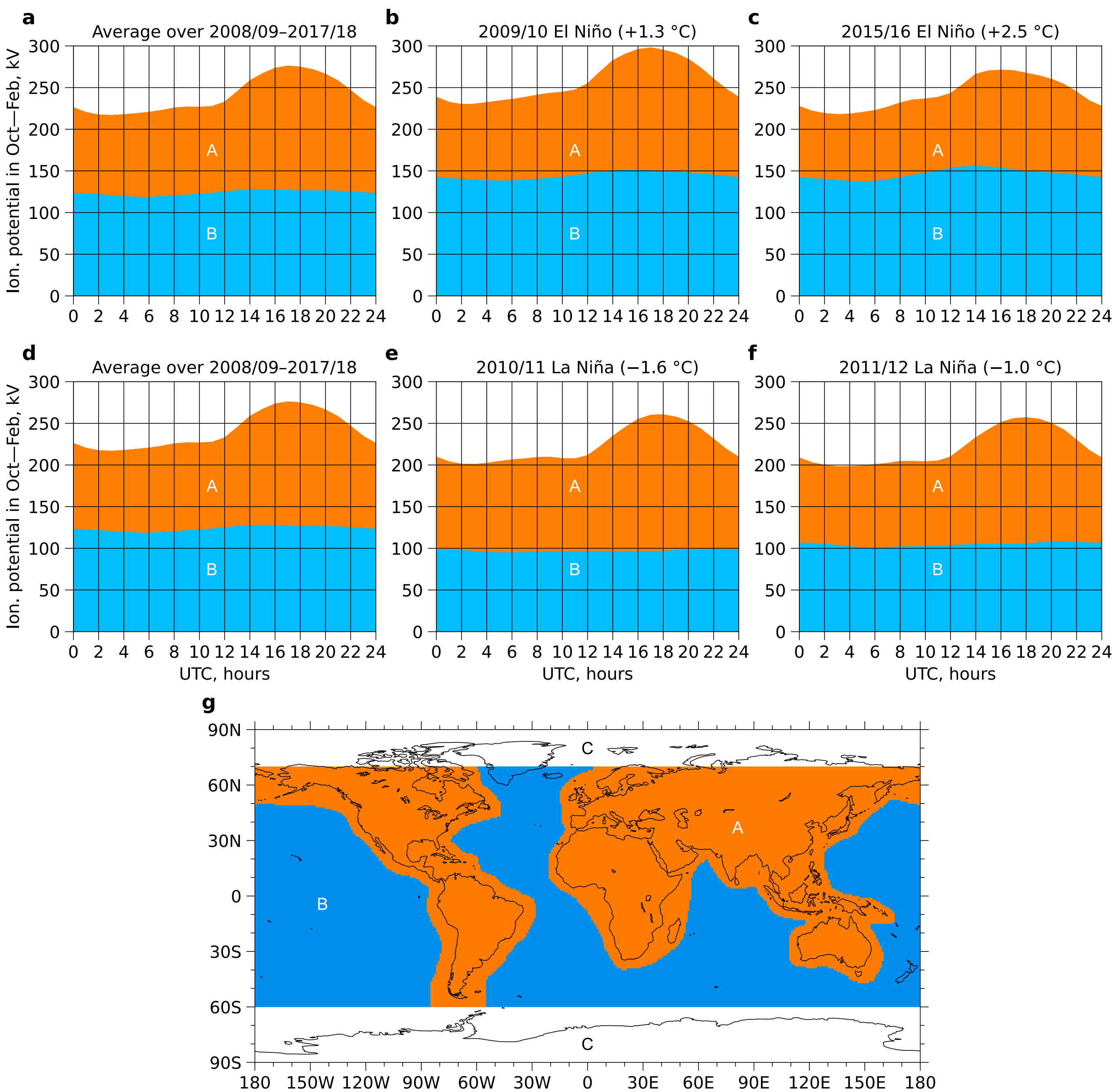

Fig. 1. (a)–(f): Diurnal variations of contributions to the ionospheric potential from land and ocean in October—February averaged over 2008/09–2017/18 (a, d; the same figure is plotted two times to facilitate comparison) and during particular strong El Niño (b, c) and La Niña (e, f) events. (g): Partition of the Earth's surface into land (A) and ocean (B). In panels (a)–(f) contributions from different regions are shown cumulatively; the colours and capital letters are chosen according to panel (g). The values in parentheses are the Niño 3.4 SST anomalies relative to the mean over 2008/09–2017/18 (see Table 1). Extremely small contribution of polar regions (C) is neglected.

in the year-to-year variability of this contribution.

3. How contributions to the GEC from land and ocean respond to ENSO

In this section we will consider contributions to the GEC from land and ocean and their changes in response to the ENSO cycle. We will look at both individual strong ENSO events and long-term variability of ENSO in general.

3.1. Changes in contributions to the GEC from land and ocean during strong El Niños and La Niñas

In Fig. 1a simulated diurnal variations of contributions to the IP from land and ocean, averaged over the ten October—February periods in 2008/09–2017/18, are shown cumulatively. The lower layer in this figure corresponds to ocean areas, and the upper layer corresponds to land areas; the corresponding parts of the Earth's surface are highlighted in Fig. 1g by the same colours and labelled by the same letters. Note that strips of surrounding water around continents are regarded as land; we also count as land oceanic regions with many large islands (namely, the Maritime Continent and Middle America). The two white strips in Fig. 1g correspond to polar regions, whose contribution to the GEC is extremely small, for which reason they are neglected. According to our simulation, the diurnal mean contributions of land and ocean are close to each other (117 kV and 123 kV respectively); at the same time it is apparent from Fig. 1a that the oceanic contribution is relatively flat whereas the contribution of land is highly variable. The latter observation agrees with inferences from satellite data (e.g., Mach et al., 2011) and expresses the fact that the diurnal cycle of convection over land is generally more pronounced than its counterpart over ocean (cf. Slyunyaev et al., 2019), largely owing to the difference of heat capacities.

Fig. 1b and c shows diurnal variations of contributions to the IP from land and ocean, averaged over October—February periods of 2009/10 and 2015/16 respectively, when strong El Niño events occurred. In other words, these two images show how the 'average' diurnal variations of contributions to the GEC presented in Fig. 1a change during strong El Niños. By looking at Fig. 1a–c, we observe that during El Niños the oceanic contribution noticeably increases for all hours of the day. At the same time the contribution of land prominently decreases for all hours of the day in the case of the 2015/16 El Niño but does not change significantly in the case of the 2009/10 El Niño. A more thorough analysis shows that in the latter case the contribution of land also decreases for nearly all hours of the day (except for 12:00–14:00 UTC), but the amount of this change does not exceed several kilovolts, which is barely noticeable in Fig. 1a and b.

Fig. 1e and f shows diurnal variations of contributions to the IP from land and ocean, averaged over October—February periods of 2010/11 and 2011/12, corresponding to strong La Niña events. For ease of comparison, we reproduced Fig. 1a in the lower row once again as Fig. 1d; comparing it with Fig. 1e and f, we see that during La Niñas the contribution of ocean markedly decreases for all hours of the day. As for the contribution of land, it slightly increases for all hours of the day in the case of the 2010/11 La Niña, while in the case of the 2011/12 La Niña there is no clear change which could be easily identified by juxtaposing Fig. 1d with Fig. 1f. A more detailed analysis shows that in this case there is a very small decrease in land contribution for 0:00–16:00 UTC and a very small increase for 17:00–23:00 UTC, with the maximum amount of change not exceeding about 3 kV.

To summarise the observations made above, we conclude that the contribution of oceans to the GEC noteably changes during ENSO events at all hours of the day, increasing in El Niño years and decreasing in La Niña years (i.e. shifting in phase with the ENSO cycle). The contribution of land behaves differently: simulations reveal a clear change in antiphase with the ENSO cycle for the 2015/16 El Niño and 2010/11 La Niña events, while for the 2009/10 El Niño and 2011/12 La Niña the land contribution remains more or less the same.

To better understand the behaviour of the land contribution to the IP, it is instructive to take into account the intensity of ENSO events which we consider here. To do so, we shall look at the SST averaged over the so-called Niño 3.4 region, defined as the area bounded by 5° N and 5° S in latitude and by 120° W and 170° W in longitude (it is common to consider various indices based on SST anomalies in the Pacific Ocean for a quantitative description of ENSO). Now that we have simulated atmospheric dynamics and contributions to the IP for the ten 5-month periods of 2008/09–2017/18, it is natural for us to calculate all anomalies with respect to the 10-year average taken over all these October—February periods combined together. For the Niño 3.4 SST this gives us a 10-year mean of 26.7 °C; calculating similar 5-month averages for individual years and subtracting this long-term mean, we obtain Niño 3.4 SST anomalies for individual years. For the four ENSO events considered in Fig. 1 these anomalies are listed in Table 1 together with the corresponding mean changes in contributions to the IP and in the total IP. Note that SSTs are not changed during individual WRF runs, hence Niño 3.4 SST values in our simulations are actually the result of transferring SSTs from the data set used for model initialisation (i.e. meteorological reanalysis data) to the WRF grid.

It is now easy to see from Table 1 that the 2015/16 El Niño is by far the most intense among the four considered events, with a Niño 3.4 SST anomaly of +2.5 °C. It should not therefore be surprising that this event is characterised by the most conspicuous change in the land contribution to the IP (see Fig. 1a and c), with a decrease of the diurnal mean by more than 20 kV. The 2010/11 La Niña is second in intensity, with an anomaly of −1.6 °C; the contribution to the IP from land responds to this event with a clear increase by about 10 kV. The two remaining events, the 2009/10 El Niño and 2011/12 La Niña, are less pronounced, being characterised by smaller SST anomalies (+1.3 °C and −1 °C respectively); we have already noted that in these cases the change in the land contribution to the GEC is relatively small, with its sign depending on the hour of the day. Moreover, whereas for the 2009/10 El Niño (+1.3 °C) we still observe that the diurnal mean contribution of land to the IP changes in antiphase with ENSO, this is not the case for the 2011/12 La Niña (−1 °C).

Thus we infer from Fig. 1 and Table 1 that during strong ENSO events the contribution of ocean varies in phase with the Niño 3.4 SST (i.e. with the ENSO cycle), while for the contribution of land we see a clear change in antiphase only in the case of very intense El Niños and La Niñas, and the effect of lesser events is uncertain. As a result of this, changes in the total IP (which is the sum of the contributions from land and ocean) in response to the Niño 3.4 SST variation, shown in the last column of Table 1, are not so easy to interpret: they have the same sign as the respective Niño 3.4 SST anomalies, but their amounts do not clearly correspond to the magnitudes of these anomalies.

3.2. Long-term dynamics of contributions to the GEC from land and ocean on the ENSO timescale

Notwithstanding that we have been able to recognise some patterns

Table 1
The Niño 3.4 SST, the diurnal mean contributions to the ionospheric potential (IP) from land, ocean and the entire Earth's surface in October—February averaged over 2008/09–2017/18 and changes in these quantites during individual strong ENSO events (see Fig. 1).

Event	Niño 3.4 SST, °C	Mean contibutions to the IP, kV		
		Land	Ocean	All Earth
Average over 2008/09–2017/18	26.7	116.9	123.1	240.0
Change during the 2009/10 El Niño	+1.3	−3.3	+20.8	+17.5
Change during the 2015/16 El Niño	+2.5	−20.5	+22.4	+1.9
Change during the 2010/11 La Niña	−1.6	+9.8	−26.8	−17.0
Change during the 2011/12 La Niña	−1.0	−0.7	−19.2	−19.9

by looking at changes in land and oceanic contributions to the IP due to ENSO events, it is difficult to make firm conclusions on the basis of only four such events present in the time span of our simulation (2008–2018). It is therefore very interesting to look at the years without prominent El Niños and La Niñas as well, focusing on the long-term dynamics of land and oceanic contributions to the GEC and their correlation with Niño 3.4 SST anomalies. We will once again concentrate on October—February periods, which are most important for the ENSO cycle.

The blue bars in Fig. 2a show the mean values of the contribution to the IP from land for October—February periods of ten successive years (in this discussion we consider only the variability of diurnal means without a detailed analysis of hourly values). The purple bars in the same figure demonstrate the year-to-year variability of the Niño 3.4 SST averaged over the same time intervals. We observe that the contribution of land has a pronounced minimum in 2015/16, corresponding to the prominent El Niño event of that year. Apart from that, the variation of the Niño 3.4 SST is not clearly reflected by the variation of the land contribution to the GEC. Despite this fact, there is still a negative correlation between these two variables, with a sample correlation coefficient $r = -0.83$.

We can estimate the significance of the observed correlation using the following fact: it is known that for two samples of size N corresponding to uncorrelated variables, the quantity $((N-2)r^2/(1-r^2))^{1/2}$, where r is the sample correlation coefficient, obeys Student's t-distribution with $N-2$ degrees of freedom, provided that these two variables follow a bivariate normal distribution; moreover, this approximately holds even for underlying distributions other than normal (Kendall and Stuart, 1961, ch. 26, 31). Having simulated all variables for $N = 10$ October—February periods of 2008/09–2017/18, we can now employ a two-tailed test on the basis of Student's t-distribution with $N-2 = 8$ degrees of freedom; such test shows that at the 5% significance level the null hypothesis that the two variables are uncorrelated is rejected if $((N-2)r^2/(1-r^2))^{1/2} \geq 2.31$ or, in other words, $|r| \geq 0.63$. A similar criterion at the 1% significance level requires that $|r| \geq 0.76$.

The discussion of the previous paragraph implies that in our situation the correlation should be considered significant at the 5% significance level if the absolute value of the sample correlation coefficient r is greater than or equal to 0.63 (for the 1% significance level this threshold value becomes 0.76); of course, we cannot hope for more when we have only ten values in each sample. In particular, this means that the negative correlation between the land contribution to the IP and Niño 3.4 SST in October—February, which we have identified above and for which $r = -0.83$, is statistically significant at the 1% level.

Fig. 2b is the counterpart of Fig. 2a for oceanic regions, comparing their contribution to the IP in different years with the same values of the Niño 3.4 SST. Here we observe a clearer relationship between the two variables, and the variability of the Niño 3.4 SST is to a large extent reproduced in the variability of the oceanic contribution to the GEC. The largest and smallest values of this contribution precisely correspond to strong El Niños and La Niñas, which we considered in Section 3.1. The sample correlation coefficient r is equal to 0.92, which means that there is a statistically significant positive correlation.

Thus when we separate the convection over the land areas from that over the oceans, we see very strong signals of opposite sign. The land areas show a strong negative correlation ($r = -0.83$) between SSTs and contributions to the GEC from land convection, while the opposite is true for the ocean convection ($r = 0.92$). In fact, the best agreement with ENSO SST variability comes from the changes in the oceanic contribution to the IP, that increases in El Niño years and decreases during La Niña years. While this may not come as a surprise, since both parameters are located over the oceans, the correlations are between SSTs in the Niño 3.4 region and *all* oceanic clouds and convection contributing to the IP.

Fig. 2c compares the year-to-year variability of the total IP (when we sum the contributions over the entire planet) and the Niño 3.4 SST. In terms of the connection between ENSO and the GEC, the results presented in this figure are misleading since there are two strong effects of opposite signs that offset each other. However, for the total IP we still observe a positive correlation with the Niño 3.4 SST, although there is no clear correspondence of maxima and minima of the IP to prominent ENSO events. The sample correlation coefficient r is just 0.49, which is not sufficient to consider the correlation significant even at the 5% significance level, but we should understand that this is probably a result of having only ten values in the sample. If we considered Decembers alone for 2008–2017 (rather than 5-month periods around Decembers for 2008/09–2017/18, as we do here), we would obtain $r = 0.68$ for the total IP (cf. Slyunyaev et al., 2021), which indicates that a significant positive correlation between ENSO and the entire GEC actually exists. At the same time in the case of Decembers we would have $r = 0.91$ for ocean (which is close to the 5-month value) and $r = -0.66$ for land (which is notably worse than the 5-month value); in general, 5-month periods yield more 'stable' results and that is the reason that we base our research on them.

In a sense, our findings regarding the total IP and Niño 3.4 SST agree with the results obtained by Harrison et al. (2011) when analysing the data of atmospheric electricity measurements at the Shetland Islands during 1968–1984. They have arrived at a positive correlation between the mean values of the fair-weather potential gradient and Niño 3.4 SST anomalies in December with a correlation coefficient of 0.64 (for a sample size of 17 years). It should also be noted that, despite this correlation, there is no clear correspondence between strong ENSO events and minima and maxima of the potential gradient (see Harrison et al., 2011, Fig. 1a), which also agrees with our inferences from Fig. 2c.

In addition to studying correlations, one can evaluate sensitivities to

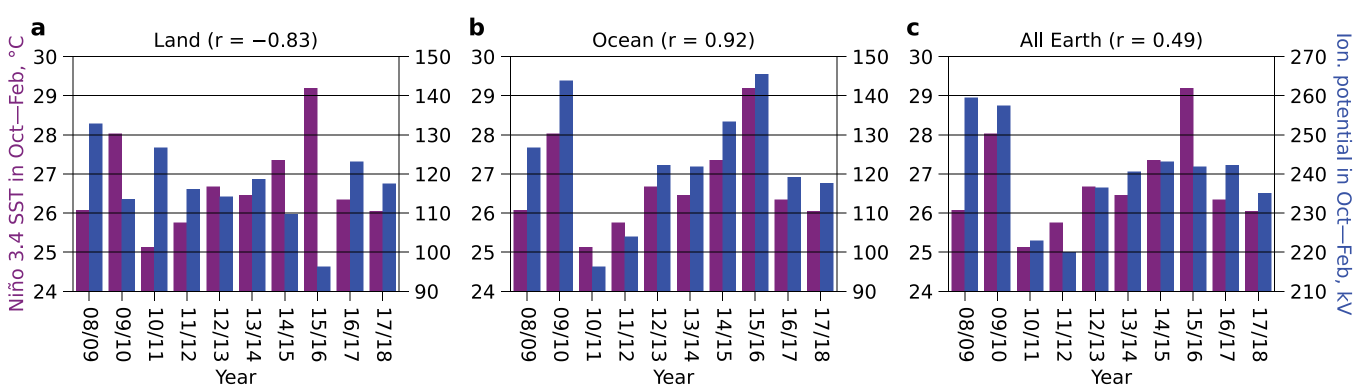

Fig. 2. The year-to-year variability of average contributions to the ionospheric potential from land (a), ocean (b) and the entire Earth's surface (c) in October—February (blue bars) and the year-to-year variability of the mean Niño 3.4 SST values for October—February (purple bars). The regions correspond to those shown in Fig. 1g. The values of the sample correlation coefficient (r) for each region are given in parentheses.

ENSO SST variability of contributions to the GEC. Fig. 3 demonstrates the data shown in Fig. 2 as scatter plots, together with the corresponding least-squares fits. From these scatter plots we deduce that the oceanic contribution to the IP (Fig. 3b) is slightly more sensitive to changes in the Niño 3.4 SST than that of land regions (Fig. 3a); in other words, the same change in the SST produces a slightly greater change in the contribution of ocean than in that of land. When we combine land and ocean, their contributions partially counterbalance each other, which makes the sensitivity of the total IP to SST variability appreciably smaller (see Fig. 3c) than individual sensitivities of land and ocean. We also observe that this sensitivity is positive, which is clear considering that land and ocean provide nearly equal contributions to the total IP (see Fig. 1 and Table 1) and the positive response to ENSO of the latter is slightly greater than the negative response of the former. In particular, this explains our earlier observation that the total IP is positively correlated with ENSO.

4. How contributions to the GEC from smaller regions respond to ENSO

In order to better understand and interpret the observations that we have made above, it is useful to look at contributions to the GEC from smaller regions than all land and all ocean combined together. We shall now discuss contributions to the IP from individual continents and oceans (or their parts).

4.1. Changes in regional contributions to the GEC during strong El Niños and La Niñas

Fig. 4a shows simulated diurnal variations of contributions to the IP from different land and oceanic regions, averaged over the ten October—February periods in 2008/09–2017/18. Different layers in this figure correspond to the regions of the Earth's surface identified in Fig. 4g by the same colours and numeric labels. Here we use the same partition of the Earth's surface into regions as that previously employed by Slyunyaev et al. (2019) to analyse regional contributions to the IP in local time. This partition comes from a further subdivision of land and ocean in Fig. 1g into smaller parts; more precisely, we divide the global land region into Europe, Africa, Northern Asia, Southern Asia, Maritime Continent, Australia, Northern America, Middle America and South America, and we distinguish Indian Ocean, western Pacific Ocean, eastern Pacific Ocean and Atlantic Ocean as parts of the global oceanic region.

The contributions of Europe, Northern Asia and Northern America are neglected in Fig. 4a, inasmuch as they are too small during Northern Hemisphere winters to be shown at this scale (their combined contribution to the IP does not exceed 0.5 kV, while the diurnal mean value of the total IP is 240 kV). We observe that the total contribution of oceans is primarily determined by the Pacific and Indian Oceans, whereas the most important regions in the total contribution of land are the Maritime Continent, South America and Africa, which roughly correspond to the three main 'chimney' regions of the GEC (Williams, 2005; Williams and Mareev, 2014).

Fig. 4b and c shows diurnal variations of the same regional contributions to the GEC, averaged over October—February periods of 2009/10 and 2015/16, when strong El Niño events occurred. Similarly, Fig. 4e and f shows these contributions for 2010/11 and 2011/12, the years corresponding to strong La Niña events, and Fig. 4d reproduces Fig. 4a in the lower row to facilitate the comparison of plots corresponding to ENSO events with the 'average' situation.

Looking at different panels of Fig. 4, we observe that the increase in the contribution of oceans to the IP during El Niños and its decrease during La Niñas are caused primarily by the behaviour of the contributions of western Pacific Ocean and eastern Pacific Ocean, both of which notably change during ENSO events in phase with the ENSO cycle. As for the contribution of land to the IP, its change in antiphase with the ENSO cycle during the most prominent ENSO events (the El Niño of 2015/16 and the La Niña of 2010/11) can be attributed to the corresponding changes in the contributions from the Maritime Continent and South America (at the same time we do not see a substantial change in the contribution of Africa). The effect on land regions of the two lesser ENSO events considered in Fig. 4 (the El Niño of 2009/10 and the La Niña of 2011/12) does not admit a simple and definite description.

4.2. Long-term dynamics of regional contributions to the GEC on the ENSO timescale

Now we shall repeat the analysis performed in Section 3.2 for smaller regions of the Earth's surface.

The blue bars in Fig. 5a–c show the year-to-year variability of mean contributions to the IP from the main land regions (the Maritime Continent, South America, Africa) in October—February; the purple bars in the same panels indicate the corresponding variation of the Niño 3.4 SST. We observe that the Maritime Continent (Fig. 5a) and South America (Fig. 5b) show a negative correlation of their contributions with ENSO SST variability. The correlation coefficients are $r = -0.79$ and $r = -0.76$ respectively, which means that the correlation is significant at the 1% significance level. It is interesting that even though the interannual variation of contributions to the GEC does not clearly reflect the SST

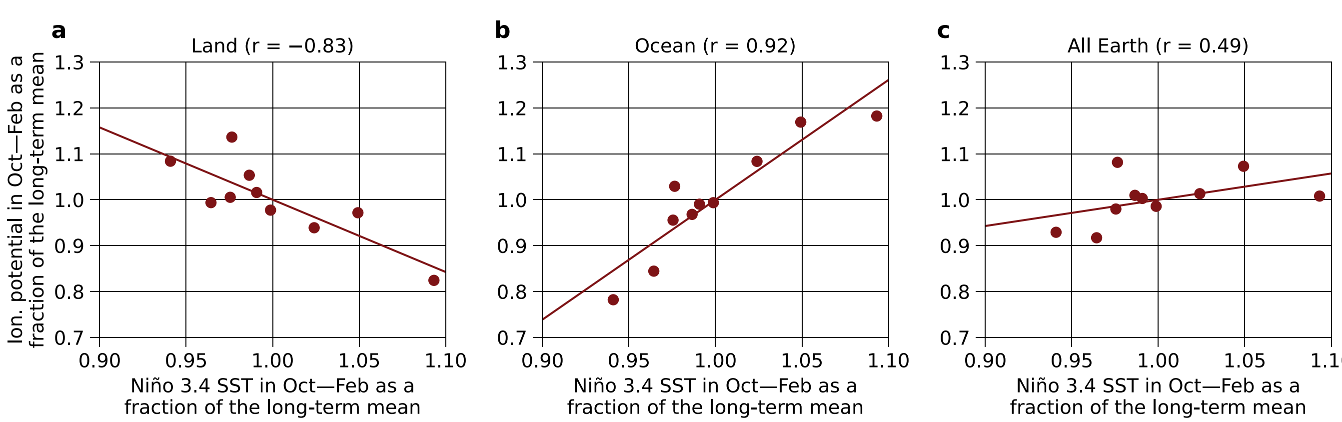

Fig. 3. The relationship between the Niño 3.4 SST values and the contributions to the ionospheric potential from land (a), ocean (b) and the entire Earth's surface (c) in October—February. The three panels show the scatter plots of the data presented in the three panels of Fig. 2. Circles correspond to individual years, straight lines represent the corresponding least-squares fits. All variables are shown as fractions of their respective long-term means (taken over all October—February periods in 2008/09–2017/18 combined together). The values of the sample correlation coefficient (*r*) for each region are given in parentheses.

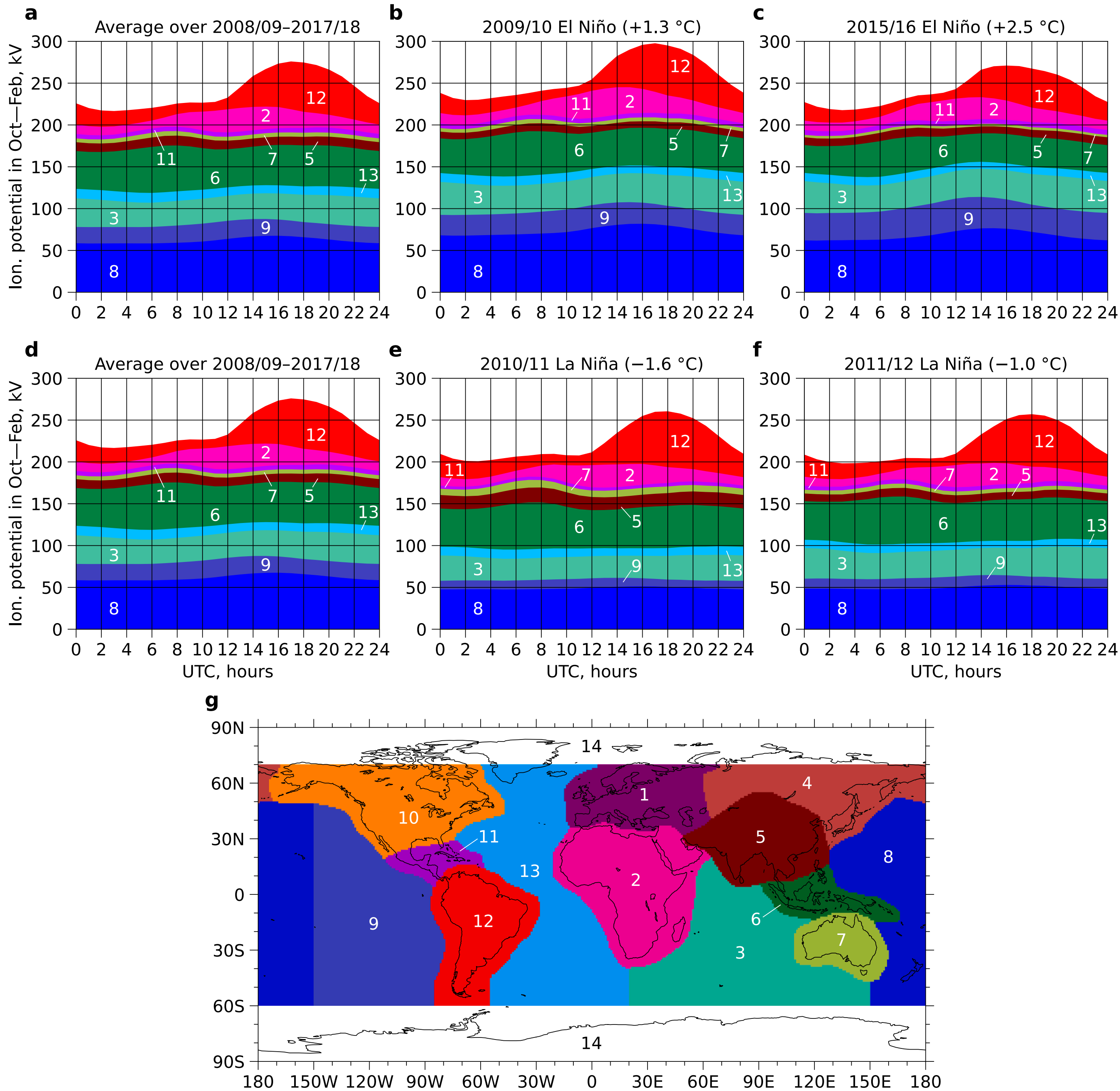

Fig. 4. (a)–(f): Diurnal variations of contributions to the ionospheric potential from different regions in October—February averaged over 2008/09–2017/18 (a, d; the same figure is plotted two times to facilitate comparison) and during particular strong El Niño (b, c) and La Niña (e, f) events. (g): Partition of the Earth's surface into regions (adapted from Slyunyaev et al., 2019): Europe (1), Africa (2), Indian Ocean (3), Northern Asia (4), Southern Asia (5), Maritime Continent (6), Australia (7), western Pacific Ocean (8), eastern Pacific Ocean (9), Northern America (10), Middle America (11), South America (12), Atlantic Ocean (13), polar regions (14). In terms of Fig. 1g, regions 1, 2, 4–7, 10–12 are considered land and regions 3, 8, 9, 12 are considered oceanic. In panels (a)–(f) contributions from different regions are shown cumulatively; the colours and numbers are chosen according to panel (g). The values in parentheses are the Niño 3.4 SST anomalies relative to the mean over 2008/09–2017/18 (see Table 1). Very small contributions from regions 1, 4, 10 and 14 cannot be shown at this scale and are neglected.

dynamics, for the particularly strong El Niño event of 2015/16 we observe clear minima in both these contributions. At the same time Africa's contribution (Fig. 5c) does not appear to be correlated with ENSO, the correlation coefficient r for it being only 0.13.

Similarly, Fig. 5d–f shows the year-to-year variability of mean contributions to the IP from the main oceanic regions (the Indian Ocean and the two parts of the Pacific Ocean) in October—February. All of these contributions appear to be positively correlated with ENSO. The contribution of the eastern Pacific Ocean (Fig. 5f) is very tightly correlated with ENSO ($r = 0.96$), which should not be surprising given that we compare contributions with the Niño 3.4 SST and the Niño 3.4 region lies in the eastern Pacific. The western Pacific Ocean (Fig. 5d) also shows a high positive correlation ($r = 0.8$), while for the Indian Ocean (Fig. 5e) the correlation coefficient is smaller ($r = 0.54$) and we cannot infer from

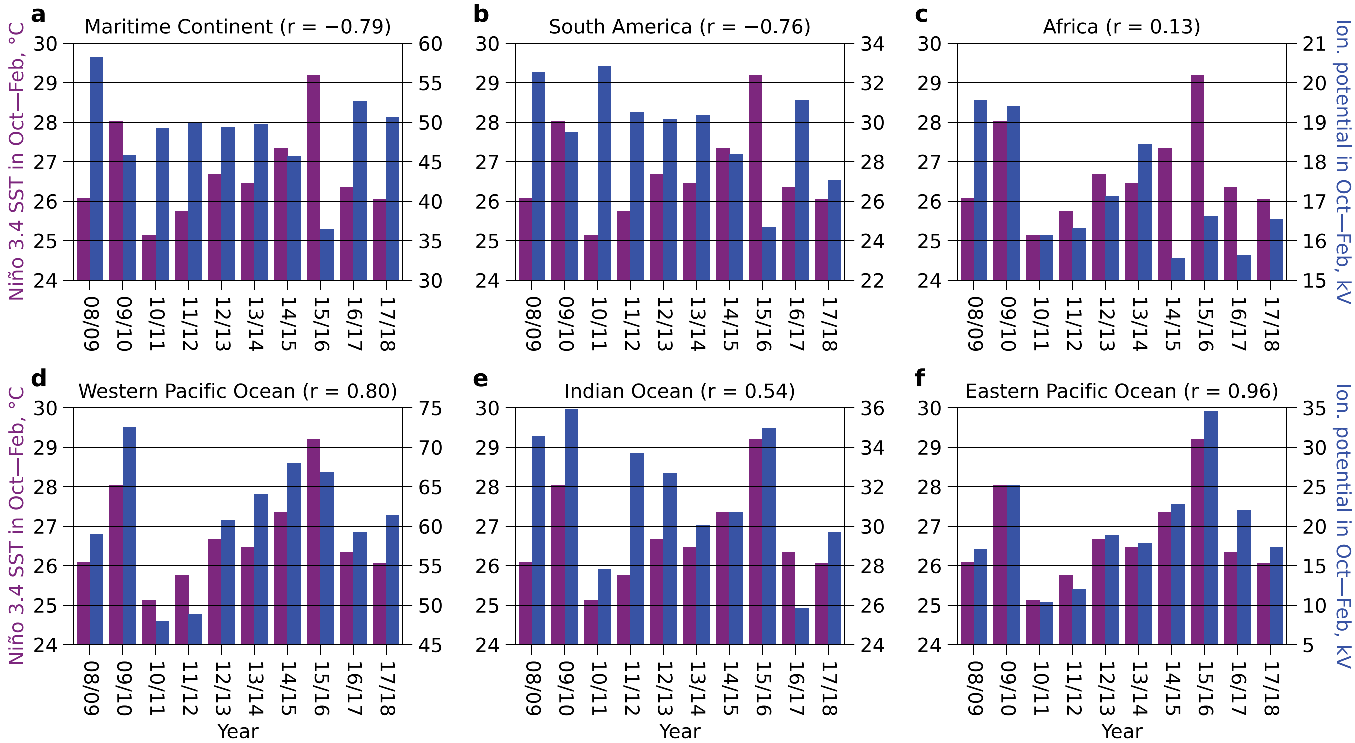

Fig. 5. The year-to-year variability of average contributions to the ionospheric potential from the most important land (a, b, c) and oceanic (d, e, f) regions in October—February (blue bars) and the year-to-year variability of the mean Niño 3.4 SST values for October—February (purple bars). The regions correspond to those shown in Fig. 4g. The values of the sample correlation coefficient (r) for each region are given in parentheses.

the data available to us that the correlation is statistically significant at the 5% level.

It is known that there are time lags up to several months between the peak of the Niño 3.4 SST and the most pronounced anomalies in atmospheric parameters (such as air temperature and precipitation) in different regions (e.g., Taschetto et al., 2020). Therefore it is likely that even though ENSO events usually peak in December, maximum changes in regional contributions to the IP may occur several months earlier or later. However, since here we always consider 5-month October—February periods around December, it is natural to expect that if the correlation between ENSO and contributions to the IP exists, we should still detect it without taking these lags into account. In addition, determining the appropriate time lag for every region which we consider would require a much more detailed discussion of ENSO beyond the scope of this study.

Thus among the main regions contributing to the GEC, the largest correlations are observed in the Maritime Continent (negative; $r = -0.79$) and in the Pacific Ocean (positive; $r = 0.8$ for the western part and $r = 0.96$ for the eastern part). This is perhaps not surprising, since this is where the ENSO signal is strongest and also the location of the measurements of the Niño 3.4 SSTs. But the sign of the correlations implies that over the Maritime continent the convection is heavily depressed during El Niño warm events, while being enhanced during La Niña cold events. On the other hand, over the Pacific the convection and contributions to the IP are enhanced in El Niño years and diminished in La Niña years. These changes in the GEC are clearly linked to the weakening (and even reversal) of the Walker circulation during El Niño events, while during La Niña events the Walker circulation is strengthened (see, e.g., Gushchina et al., 2020, Fig. 4). In addition, over South America (east of the Andes) we see a negative correlation ($r = -0.76$) between the contributions to the IP and SSTs. Warmer SSTs during El Niño years result in enhanced subsidence over the Amazon due to changes in the Walker circulation, and hence less convection and thunderstorms forming over South America in general during El Niño years, and the opposite in La Niña years.

To summarise the discussion above, changes in the Walker circulation during El Niño events result in increased rising motion over the Pacific Ocean and significant sinking motion over the Maritime Continent, as well as over North East Brazil and the Amazon; this leads to enhanced convection over the Pacific Ocean and depressed convection over the Maritime Continent and South America during El Niños (the opposite is true during La Niñas). Considering that the Pacific Ocean dominates the oceanic contribution to the IP, whereas the Maritime Continent and South America to a large extent determine the land contribution (see Fig. 4), this provides an explanation for our earlier observation that in terms of contributions to the IP, land and oceans respond oppositely to the ENSO cycle (see Figs. 2 and 3).

Fig. 6a–f demonstrates the data shown in Fig. 5a–f in the form of scatter plots. The least-squares fits to the data shown in the same panels allow us to describe the sensitivity of contributions to the IP from different regions to changes in the Niño 3.4 SST (or, in other words, to ENSO). We observe that the contribution of the eastern Pacific Ocean, where the Niño 3.4 region is located, to the GEC (Fig. 6f) is by far the most sensitive to the ENSO cycle among the main regions maintaining the GEC. However, as one can infer from Fig. 4, this region gives a rather small portion of the total IP. The Maritime Continent (Fig. 6a) and western Pacific Ocean (Fig. 6d) show slightly higher sensitivity than South America (Fig. 6b) and the Indian Ocean (Fig. 6e). The contribution of Africa (Fig. 6c) has the smallest sensitivity among the regions considered in the figure, as we might have expected from the lack of correlation.

Fig. 7a–g shows the year-to-year variability of the mean contributions to the IP from the remaining regions of the Earth’s surface (according to Fig. 4) in October—February. For the Atlantic Ocean (Fig. 7a) we do not see a clear relationship with ENSO ($r = -0.17$). The contributions from Southern Asia (Fig. 7b) and Australia (Fig. 7a) behave

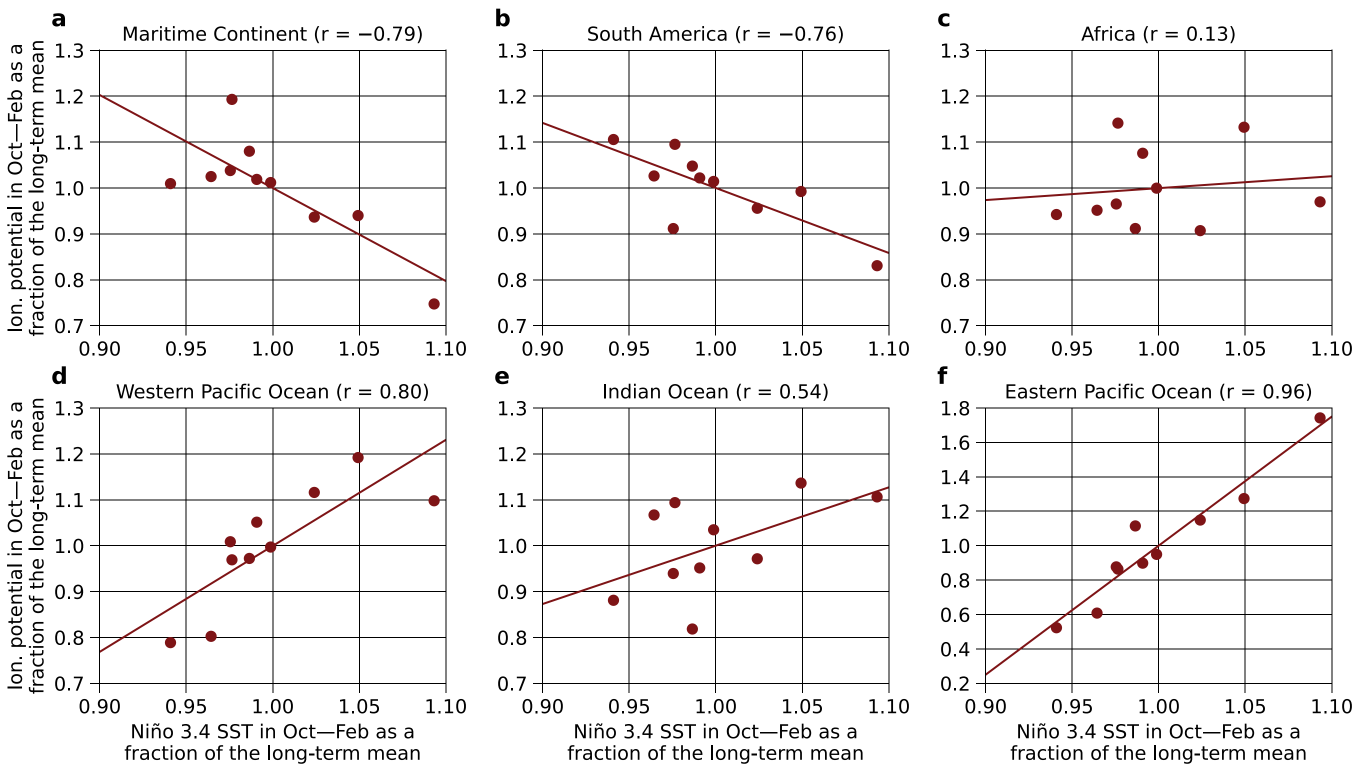

Fig. 6. The relationship between the Niño 3.4 SST values and the contributions to the ionospheric potential from the most important land (a, b, c) and oceanic (d, e, f) regions in October—February. The six panels show the scatter plots of the data shown in the six panels of Fig. 5. Circles correspond to individual years, straight lines represent the corresponding least-squares fits. All variables are shown as fractions of their respective long-term means (taken over all October—February periods in 2008/09–2017/18 combined together). The values of the sample correlation coefficient (r) for each region are given in parentheses.

similarly to the Maritime Continent, as one might have expected: they show a negative correlation with the Niño 3.4 SST. For Australia this correlation is statistically significant at the 5% level ($r = -0.71$), while in the case of Southern Asia we do not have enough data for such conclusion ($r = -0.59$). The contribution of Northern America (Fig. 7e) is positively correlated with ENSO ($r = 0.72$), but during Northern Hemisphere winter it is very small compared to those of other regions, according to our simulation. Note, however, that we include in each land region a surrounding oceanic strip, which may yield a considerable contribution in this case. Lying between South America with a high negative correlation and Northern America with a high positive correlation, Middle America (Fig. 7c) shows a moderate positive correlation with the Niño 3.4 SST, but the correlation coefficient is notably smaller ($r = 0.43$), which is insufficient to show the statistical significance. It is likely that here the proximity of ocean also plays an important part. Finally, the contributions from Europe (Fig. 7f) and Northern Asia (Fig. 7g) are even smaller in October—February than that of Northern America, and we do not see any clear relationship between these contributions and ENSO ($r = 0.11$ for Europe and $r = -0.35$ for Northern Asia).

Summarising the information inferred from Figs. 5 and 7, we can conclude that contributions from the Pacific are positively correlated with ENSO, while contributions from South America and contributions from the region including Southern Asia, the Maritime Continent and Australia are negatively correlated with ENSO. For other regions either the situation is unclear or their contributions in Northern Hemisphere winters are negligible. Let us also note that virtually every region (perhaps except for the eastern Pacific Ocean) does not precisely reproduce the ENSO cycle in the variability of its contributions to the GEC.

Finally, we want to make another interesting observation. We have already noted that the diurnal mean total IP has a positive sensitivity to Niño 3.4 SST anomalies (Fig. 3c) owing to the fact that the contribution of oceans is slightly more sensitive to ENSO than that of land. On the other hand, the diurnal maximum of the IP is determined by South America (Fig. 4), whose contribution has a negative sensitivity to ENSO (Fig. 6b). Therefore it is natural to expect that the diurnal peak-to-peak amplitude of the IP will also change in antiphase with the ENSO cycle. This effect should be even more significant for the *relative* peak-to-peak amplitude—that is to say, the peak-to-peak amplitude divided by the diurnal mean—since the numerator should generally decrease with increasing SST, when the denominator generally increases.

By comparing Fig. 4c and e, corresponding to very strong ENSO events, with Fig. 4a (or Fig. 4d), corresponding to the long-term average, we observe that these two events illustrate the idea suggested above. In the 'average' situation we have the IP variation with the diurnal mean value of 240 kV and the peak-to-peak amplitude of 59.2 kV, which constitutes 25% of the mean. During the 2015/16 El Niño the diurnal mean IP increases to 242 kV, while the amplitude decreases to 53.2 kV, or 22% of the mean. On the other hand, during the 2010/11 La Niña the diurnal mean IP decreases to 223 kV, whereas the amplitude slightly increases and reaches 59.6 kV; this produces the relative peak-to-peak amplitude of 27% of the mean. Thus we observe that during a strong El Niño the Carnegie curve becomes flatter, while during a strong La Niña its variation becomes more pronounced. However, this is a rather subtle effect and one should not expect to observe it for any particular ENSO event (just as we have seen that the variability of the land contribution to the GEC does not precisely follow the variability of the Niño 3.4 SST). For example, for lesser ENSO events of 2009/10 and 2011/12 (Fig. 4b and f) we do not see clear changes in the peak-to-peak amplitude in accordance with ENSO. A more detailed discussion of the response of the shape of the Carnegie curve to the ENSO cycle can be found in Slyunyaev et al. (2021).

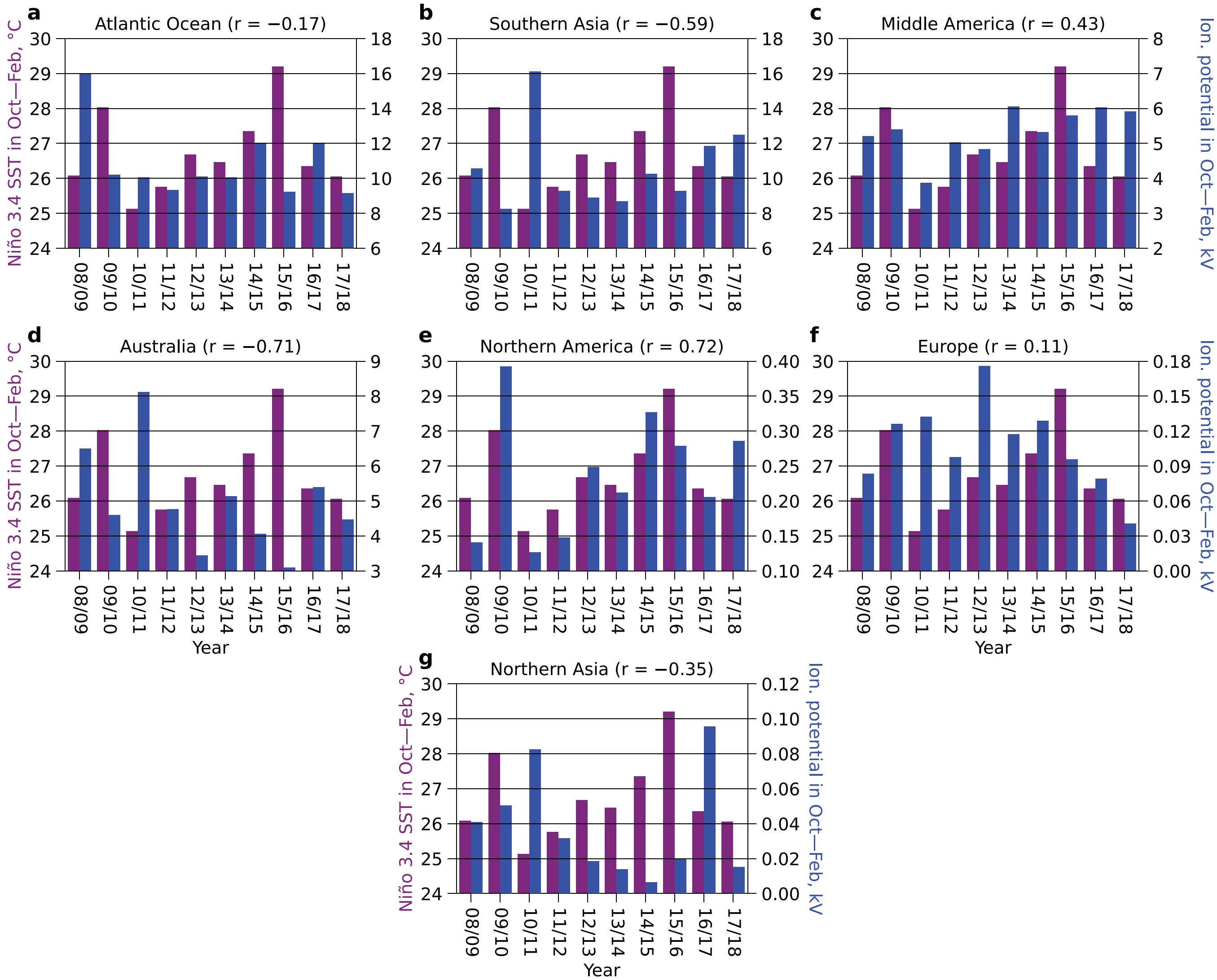

Fig. 7. Similar to Fig. 5 for regions with smaller contributions shown in Fig. 4g.

5. Spatial variations of contributions to the GEC during the 2015/16 El Niño

Now we shall investigate in more detail how the spatial distribution of contributions to the GEC changes during strong ENSO events. We shall restrict our attention to the 2015/16 El Niño, which is by far the strongest event among those which occurred during 2008–2018 (see Table 1 and Fig. 1).

5.1. Diurnal mean changes

Fig. 8a demonstrates the geographical distribution of diurnal mean contributions to the IP from individual grid columns, averaged over the ten October—February periods in 2008/09–2017/18. Recall that we use a $1^\circ \times 1^\circ$ latitude-longitude grid and that we have normalised the IP such that the sum of these averaged contributions is equal to 240 kV. Although the areas of $1^\circ \times 1^\circ$ cells vary with latitude, this variation is not very pronounced between 30° S and 30° N, where the majority of GEC generators lie. This means that we can neglect this variability of surface areas when comparing contributions to the GEC from different grid columns.

Fig. 8b indicates how the contributions shown in Fig. 8a changed during the very strong El Niño of 2015/16. Although for this particular El Niño the total IP changed only by 1.9 kV, we have already noted that this is a sum of much greater changes in land and ocean contributions to the IP offsetting each other (see Table 1). This behaviour is further illustrated in Fig. 8b, where we observe substantial changes in regional contributions of both signs. The most pronounced changes occur over South America, over and around the Maritime Continent and in the equatorial oceans, especially over the Pacific. More precisely, we observe a general enhancement of contributions to the IP from the equatorial region in the eastern Pacific Ocean (in particular, in a neighbourhood of the Niño 3.4 region which we consider here) and a general reduction of contributions from the Maritime Continent and South America.

5.2. Hourly changes

In order to better understand the geographical distribution of contributions to the GEC, it is useful to look not only at their diurnal means but also at their hourly values. Fig. 9a–d and Fig. 10a–d show the geographical distribution of contributions to the IP from individual grid columns at different hours of the day. By looking at these figures, it is easy to identify the diurnal variation of regional contributions. It is known that while land regions produce maximum contributions to the GEC around 16:00 local time, contributions of oceanic regions reach maxima around 4:00 local time (see Slyunyaev et al., 2019). It is interesting that for the Maritime Continent we see a 'superposition' of these two principles with the maxima of contributions from land and ocean at different hours (compare Fig. 9d with Fig. 10d).

Figs. 9e–h and 10e–h show the geographical distribution of changes in contributions to the IP from individual grid columns at different hours of the day during the 2015/16 El Niño. These figures give us a detailed picture of the behaviour of contributions from South America, Africa, the Maritime Continent and the oceans during a strong El Niño event.

Oceanic convection in the Pacific is related to the shift in the Walker circulation during El Niño years. The warm ocean waters in the Niño 3.4 region result in the focusing of the convection along the equator. We see that in the central Pacific along the equator the convection is enhanced, while north and south of the equator the convection is diminished. The conclusion is that the enhanced convergence of moisture and heat along the equator in El Niño years results in enhanced, more compact convection that leads to an increase in the oceanic contribution to the IP.

On the other hand, the contributions of South America and the Maritime Continent decrease during a strong El Niño. For South America, this decrease is most conspicuous at the same hours when this contribution itself is most prominent, namely during 15:00–21:00 UTC (see Fig. 10f–h). In contrast to that, over the Maritime Continent we observe a general decrease in contributions to the GEC at all hours of the day. Note that although in this study we regard the Maritime Continent as land, the negative response to ENSO of its contribution to the GEC is primarily determined by the oceanic part of this region. At the same time we can identify no clear trend in the variability of convection over Africa during El Niño. The small impact of ENSO on Africa is probably caused by the fact that Africa is furthest from the Pacific ocean, where the ENSO SST signals are strongest.

6. Discussion and conclusions

Our study uses the IP as a global index characterising the GEC intensity. It involves all electrified clouds globally as defined earlier. The IP is different from thunderstorms and lightning since it also includes electrified clouds that contribute to the GEC but do not necessarily have lightning. Hence, our study is different to previous studies that looked at the link between ENSO and lightning activity in different regions of the globe. The IP is better linked to global electrified convective clouds which also occur over the oceans, even though they often do not produce lightning.

Our study shows for the first time the spatial contribution from clouds in different parts of the globe to the IP. Using a global model with the calculation of the IP contribution in each model pixel allows us to understand the contribution of different regions of the globe to the GEC on timescales of the ENSO. From our analysis we find that the oceans and land areas respond oppositely to changes in SSTs as related to ENSO. During El Niño years there are large increases in convective cloud area over the oceans, while large decreases are observed over the tropical land areas (particularly the Amazon and the Maritime continent); the opposite is true during La Niña years. In terms of the GEC this means that contributions to the IP from the Pacific are positively correlated with ENSO, while contributions from South America and the region including Southern Asia, the Maritime Continent and Australia are negatively correlated with ENSO. These changes and differences between land and ocean convection are clearly linked to shifts and changes in the east—west Walker circulation cells that will decrease the convection of land during El Nino years, while increasing the convection over the oceans. However, when integrating over the globe, these two opposing effects for land and oceans nearly cancel each other out.

It is interesting that when we look at the whole Earth, we still observe a positive correlation between the total IP and the Niño 3.4 SST. As we have already explained, we do not have enough data to show that this correlation is significant, since in this case the correlation coefficient is smaller than those for land and ocean, but we can be sure that the total IP is indeed linked to ENSO, as we do obtain a statistically significant correlation when we consider Decembers alone instead of 5-month periods around Decembers. According to our analysis, this positive relationship between the total IP and ENSO is the result of the fact that the oceanic contribution to the GEC is slightly more sensitive to ENSO than the land contribution, while these two contributions are close to each other. In particular, this implies that it is crucially important to consider the contribution of oceans when discussing the GEC and its generators. If nearly all of the IP were generated by convection over land, we would likely see a negative correlation between the GEC intensity and Niño 3.4 SST, while the results inferred by Harrison et al. (2011) from atmospheric electric field measurements agree with our simulations, indicating that the opposite is true.

Finally, let us note that despite the fact that we have been able to identify definite links between the ENSO cycle and the GEC, there are some issues that require further investigation. This study is based on the results of simulating the atmospheric dynamics for 2008–2018; therefore we were able to analyse only ten October—February periods

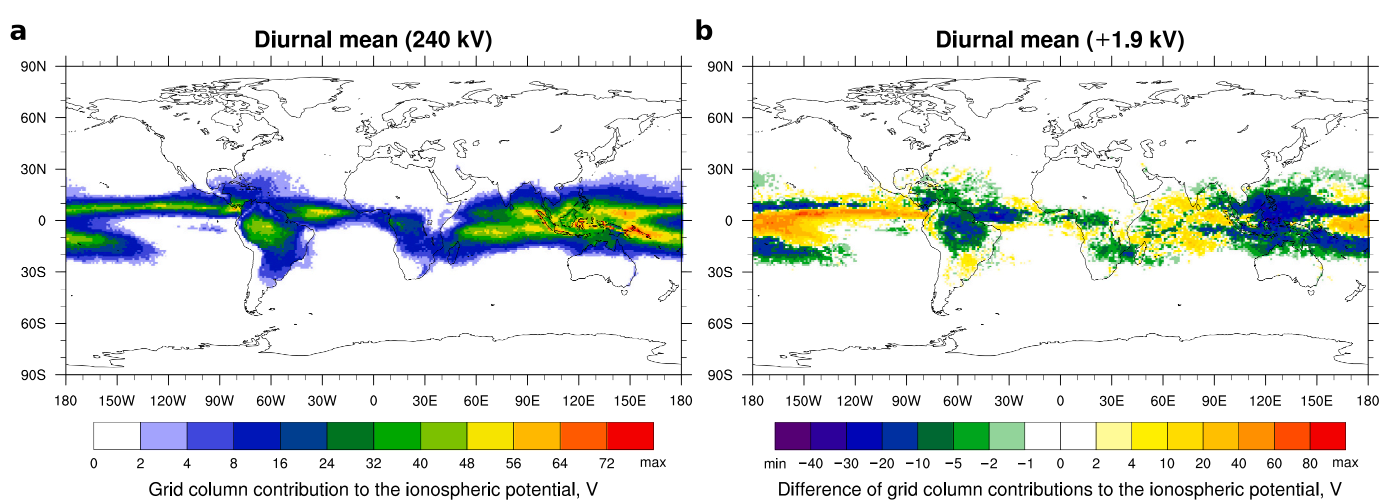

Fig. 8. (a): Diurnal mean contributions to the ionospheric potential from individual grid columns averaged over the ten October—February periods in 2008/09–2017/18. (b): Changes in diurnal mean contributions to the ionospheric potential from individual grid columns in October 2015 — February 2016 relative to the corresponding long-term averages shown in the left column. The values in parentheses represent the total ionospheric potential (in panel (a)) or its change (in panel (b)).

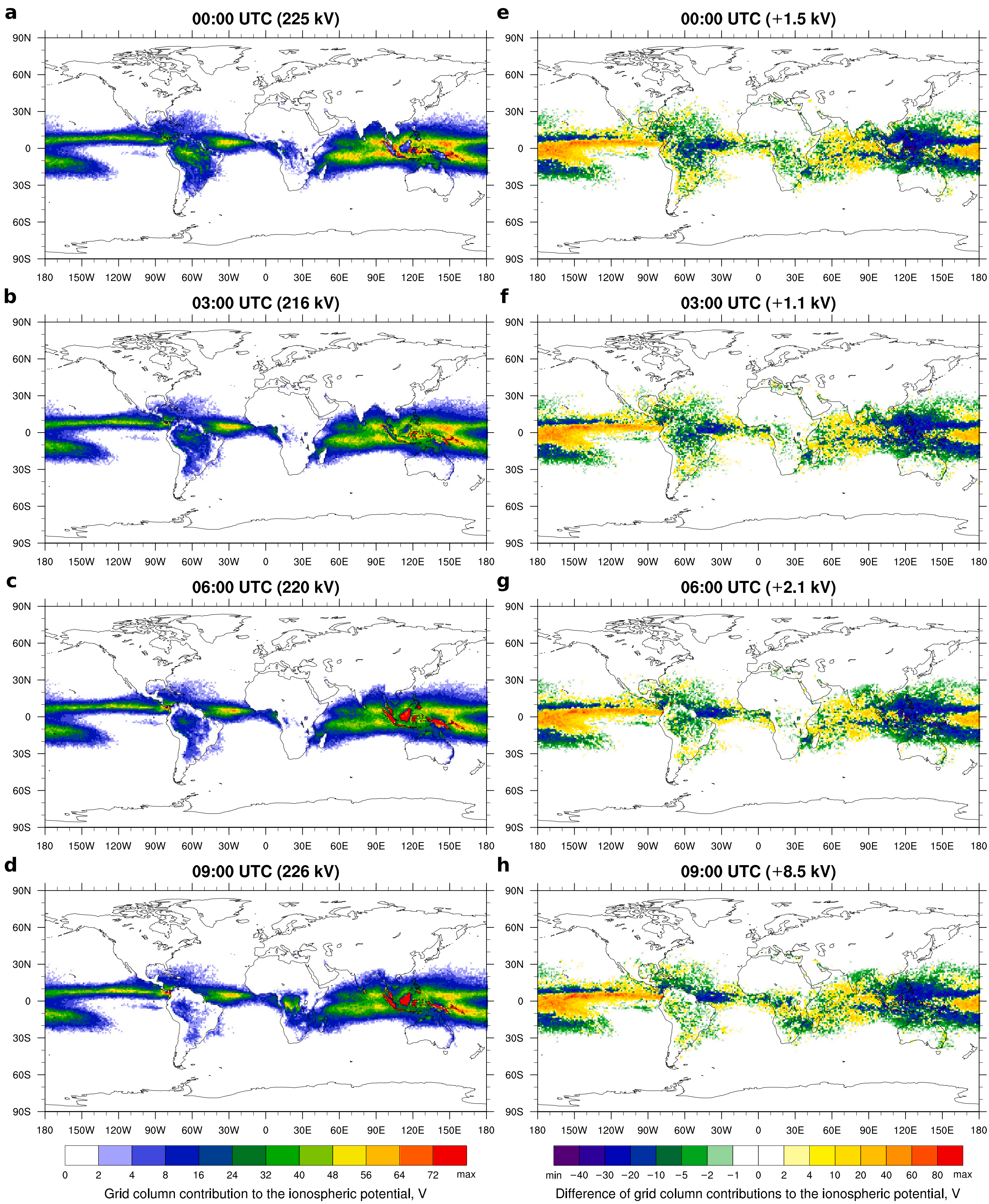

Fig. 9. (a)–(d): Contributions to the ionospheric potential from individual grid columns averaged over the ten October—February periods in 2008/09–2017/18. (e)–(h): Changes in contributions to the ionospheric potential from individual grid columns in October 2015 — February 2016 relative to the corresponding long-term averages shown in the left column. The four rows correspond to 0:00, 3:00, 6:00 and 9:00 UTC. The values in parentheses represent the total ionospheric potential (in panels (a)–(d)) or its change (in panels (e)–(h)).

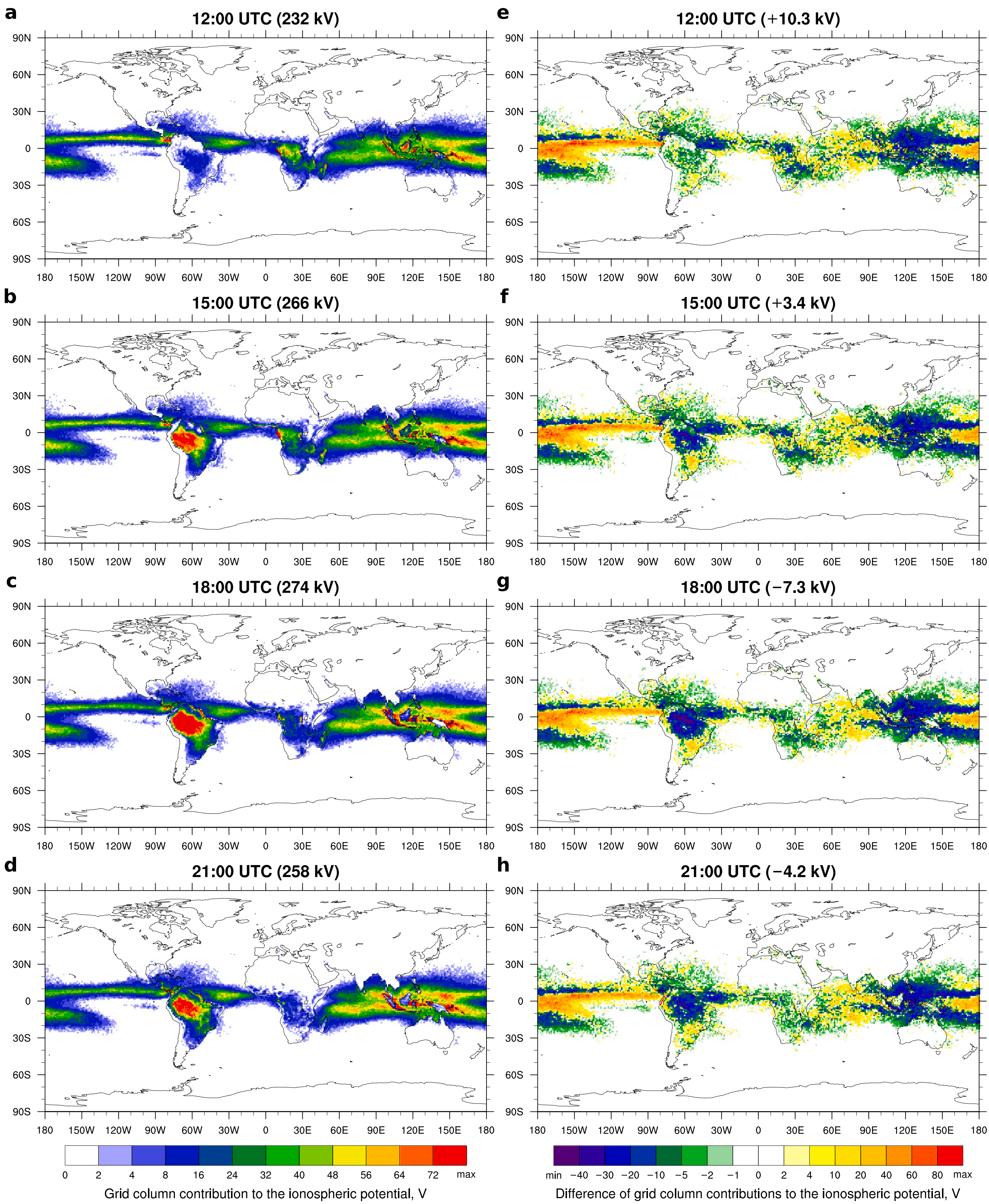

Fig. 10. Similar to Fig. 9 for 12:00, 15:00, 18:00 and 21:00 UTC.

covering just four relatively strong El Niños and La Niñas. These limitations affected some aspects of our analysis; for instance, the small sample size (ten winter seasons) made it impossible to determine the statistical significance of the observed correlations except for the strongest ones. Another example is the behaviour of contributions to the GEC during ENSO events: we have seen that the oceanic contribution always clearly responds to changes in the Niño 3.4 SST during El Niños and La Niñas, whereas the land contribution changes in a clear manner only in case of very strong events. However, it is difficult to make firm conclusions on the basis of only four events which we considered, and a longer time series is needed to completely understand this relationship. Also, such time series should make it possible to analyse time lags existing between the peaks of ENSO events and the corresponding changes in atmospheric parameters (and, by inference, changes in contributions to the GEC). Therefore it is likely that further studies will provide more information about the links revealed in this study.

Declaration of competing interest

The authors declare that they have no known competing financial interests or personal relationships that could have appeared to influence the work reported in this paper.

Acknowledgements

The investigation presented in Sections 2 and 3 (including the development of the technique for GEC simulation) was supported by the Russian Science Foundation (project no. 18-77-10061). The work presented in Sections 4 and 5 was supported by a grant from the Government of the Russian Federation (contract no. 075-15-2019-1892). The WRF model can be downloaded from https://www2.mmm.ucar.edu/wrf/users/downloads.html. To initialise the WRF model, we used the NCEP FNL Operational Model Global Tropospheric Analyses data set, which is available at https://rda.ucar.edu/datasets/ds083.2. Source codes and scripts used to analyse the results of simulation and plot the images are available at https://bitbucket.org/nilyin/enso-gec-2020.

Appendix A. Parameterisation of the IP

To express the IP V in terms of climate variables, we use the following formula, suggested by Slyunyaev et al. (2019) as a development of an earlier parameterisation by Mareev and Volodin (2014):

$$V = \sum_i \frac{j_0 H S_i}{\sigma_0 S_\mathrm{E}} \frac{P_i}{W_i} \left(\exp\left(-\frac{z_i^\mathrm{l}}{H} \right) - \exp\left(-\frac{z_i^\mathrm{u}}{H} \right) \right) \times \begin{cases} 0, & \varepsilon_i < \varepsilon_0, \\ 1, & \varepsilon_i \geq \varepsilon_0, \end{cases} \tag{A.1}$$

where the sum is taken over all grid columns and in the ith column S_i is the Earth's surface area, W_i is the total amount of precipitable water, P_i is the amount of precipitation totalled over a symmetric two-hour interval, z_i^l and z_i^u are the heights of the 0 °C and −38 °C isotherms (approximating the lower and upper boundaries of the mixed phase region) and ε_i is the maximum convective available potential energy (CAPE). Other parameters have the following meaning: S_E is the total area of the Earth's surface (equal to the sum of all S_i), σ_0 is the average conductivity at the Earth's surface, $H = 6$ km is the average scale height for the conductivity, $\varepsilon_0 = 1$ kJ/kg is a threshold CAPE value and j_0 is the characteristic value of the charge separation current density inside electrified clouds. For the derivation of Eq. (A.1) and a discussion of the choice of the main parameters, see Ilin et al. (2020).

References

Goodman, S.J., Buechler, D.E., Knupp, K., Driscoll, K., McCaul Jr., E.W., 2000. The 1997–98 El Nino event and related wintertime lightning variations in the southeastern United States. Geophys. Res. Lett. 27, 541–544. https://doi.org/10.1029/1999GL010808.

Gushchina, D., Zheleznova, I., Osipov, A., Olchev, A., 2020. Effect of various types of ENSO events on moisture conditions in the humid and subhumid tropics. Atmosphere 11, 1354. https://doi.org/10.3390/atmos11121354.

Hamid, E.Y., Kawasaki, Z., Mardiana, R., 2001. Impact of the 1997–98 El Niño Event on lightning activity over Indonesia. Geophys. Res. Lett. 28, 147–150. https://doi.org/10.1029/2000GL011374.

Harrison, R.G., 2013. The Carnegie curve. Surv. Geophys. 34, 209–232. https://doi.org/10.1007/s10712-012-9210-2.

Harrison, R.G., Joshi, M., Pascoe, K., 2011. Inferring convective responses to El Niño with atmospheric electricity measurements at Shetland. Environ. Res. Lett. 6, 044028 https://doi.org/10.1088/1748-9326/6/4/044028.

Ilin, N.V., Slyunyaev, N.N., Mareev, E.A., 2020. Toward a realistic representation of global electric circuit generators in models of atmospheric dynamics. J. Geophys. Res. Atmos. 125 https://doi.org/10.1029/2019JD032130 e2019JD032130.

Jánský, J., Lucas, G.M., Kalb, C., Bayona, V., Peterson, M.J., Deierling, W., Flyer, N., Pasko, V.P., 2017. Analysis of the diurnal variation of the global electric circuit obtained from different numerical models. J. Geophys. Res. Atmos. 122, 12906–12917. https://doi.org/10.1002/2017JD026515.

Kalb, C., Deierling, W., Baumgaertner, A., Peterson, M., Liu, C., Mach, D., 2016. Parameterizing total storm conduction currents in the Community Earth System Model. J. Geophys. Res. Atmos. 121, 13715–13734. https://doi.org/10.1002/2016JD025376.

Kendall, M.G., Stuart, A., 1961. The Advanced Theory of Statistics. Volume 2: Inference and Relationship. Charles Griffin & Co. Ltd., London.

Lucas, G.M., Baumgaertner, A.J.G., Thayer, J.P., 2015. A global electric circuit model within a community climate model. J. Geophys. Res. Atmos. 120, 12054–12066. https://doi.org/10.1002/2015JD023562.

Mach, D.M., Blakeslee, R.J., Bateman, M.G., Bailey, J.C., 2010. Comparisons of total currents based on storm location, polarity, and flash rates derived from high-altitude aircraft overflights. J. Geophys. Res. 115 https://doi.org/10.1029/2009JD012240.

Mach, D.M., Blakeslee, R.J., Bateman, M.G., 2011. Global electric circuit implications of combined aircraft storm electric current measurements and satellite-based diurnal lightning statistics. J. Geophys. Res. 116, D05201 https://doi.org/10.1029/2010JD014462.

Mareev, E.A., Volodin, E.M., 2014. Variation of the global electric circuit and ionospheric potential in a general circulation model. Geophys. Res. Lett. 41, 9009–9016. https://doi.org/10.1002/2014GL062352.

Markson, R., 1986. Tropical convection, ionospheric potentials and global circuit variation. Nature 320, 588–594. https://doi.org/10.1038/320588a0.

Markson, R., 2007. The global circuit intensity: its measurement and variation over the last 50 years. Bull. Amer. Meteor. Soc. 88, 223–241. https://doi.org/10.1175/BAMS-88-2-223.

Markson, R., Ruhnke, L.H., Williams, E.R., 1999. Global scale comparison of simultaneous ionospheric potential measurements. Atmos. Res. 51, 315–321. https://doi.org/10.1016/S0169-8095(99)00016-2.

McPhaden, M.J., Santoso, A., Cai, W., 2020. El Niño Southern Oscillation in a Changing Climate. John Wiley & Sons, Inc.—American Geophysical Union, Hoboken, NJ. https://doi.org/10.1002/9781119548164. Geophysical Monograph Series 253.

National Centers for Environmental Prediction, National Weather Service, NOAA and U. S. Department of Commerce, 2000. NCEP FNL Operational Model Global Tropospheric Analyses, Continuing from July 1999. Research Data Archive at the National Center for Atmospheric Research, Computational and Information Systems Laboratory, Boulder, CO, USA. https://doi.org/10.5065/D6M043C6 (updated daily).

Price, C., 2009. Will a drier climate result in more lightning? Atmos. Res. 91, 479–484. https://doi.org/10.1016/j.atmosres.2008.05.016.

Price, C., Federmesser, B., 2006. Lightning-rainfall relationships in Mediterranean winter thunderstorms. Geophys. Res. Lett. 33, L07813 https://doi.org/10.1029/2005GL024794.

Rycroft, M.J., Israelsson, S., Price, C., 2000. The global atmospheric electric circuit, solar activity and climate change. J. Atmos. Sol. Terr. Phys. 62, 1563–1576. https://doi.org/10.1016/S1364-6826(00)00112-7.

Sátori, G., Zieger, B., 1999. El Niño related meridional oscillation of global lightning activity. Geophys. Res. Lett. 26, 1365–1368. https://doi.org/10.1029/1999GL900264.
Sátori, G., Williams, E., Lemperger, I., 2009. Variability of global lightning activity on the ENSO time scale. Atmos. Res. 91, 500–507. https://doi.org/10.1016/j.atmosres.2008.06.014.
Skamarock, W.C., Klemp, J.B., Dudhia, J., Gill, D.O., Barker, D., Duda, M.G., Huang, X., Wang, W., Powers, J.G., 2008. A Description of the Advanced Research WRF Version 3. NCAR Technical Note NCAR/TN-475+STR. https://doi.org/10.5065/D68S4MVH.
Slyunyaev, N.N., Ilin, N.V., Mareev, E.A., 2019. Modeling contributions of continents and oceans to the diurnal variation of the global electric circuit. Geophys. Res. Lett. 46, 5516–5525. https://doi.org/10.1029/2019GL083166.
Slyunyaev, N.N., Ilin, N.V., Mareev, E.A., Price, C.G., 2021. A new link between El Niño—Southern Oscillation and atmospheric electricity. Environ. Res. Lett. 16, 044025 https://doi.org/10.1088/1748-9326/abe908.
Taschetto, A.S., Ummenhofer, C.C., Stuecker, M.F., Dommenget, D., Ashok, K., Rodrigues, R.R., Yeh, S.W., 2020. ENSO atmospheric teleconnections. In: McPhaden, M.J., Santoso, A., Cai, W. (Eds.), El Niño Southern Oscillation in a Changing Climate. John Wiley & Sons, Inc.—American Geophysical Union, Hoboken, NJ, pp. 311–335. https://doi.org/10.1002/9781119548164.ch14. Geophysical Monograph Series 253.
Tinsley, B.A., 2008. The global atmospheric electric circuit and its effects on cloud microphysics. Rep. Prog. Phys. 71, 066801 https://doi.org/10.1088/0034-4885/71/6/066801.
Tsonis, A.A., Elsner, J.B., Hunt, A.G., Jagger, T.H., 2005. Unfolding the relation between global temperature and ENSO. Geophys. Res. Lett. 32, L09701 https://doi.org/10.1029/2005GL022875.
Villafuerte II, M.Q., Matsumoto, J., 2015. Significant influences of global mean temperature and ENSO on extreme rainfall in Southeast Asia. J. Clim. 28, 1905–1919. https://doi.org/10.1175/JCLI-D-14-00531.1.
Whipple, F.J.W., Scrase, F.J., 1936. Point discharge in the electric field of the Earth: an analysis of continuous records obtained at Kew Observatory. Lond. Geophys. Mem. 68.
Williams, E.R., 2005. Lightning and climate: a review. Atmos. Res. 76, 272–287. https://doi.org/10.1016/j.atmosres.2004.11.014.
Williams, E., Mareev, E., 2014. Recent progress on the global electrical circuit. Atmos. Res. 135–136, 208–227. https://doi.org/10.1016/j.atmosres.2013.05.015.
Wilson, C.T.R., 1921. Investigations on lightning discharges and on the electric field of thunderstorms. Phil. Trans. Roy. Soc. Lond. A 221, 73–115. https://doi.org/10.1098/rsta.1921.0003.
Wilson, C.T.R., 1924. The electric field of a thundercloud and some of its effects. Proc. Phys. Soc. Lond. 37, 32D–37D. https://doi.org/10.1088/1478-7814/37/1/314.